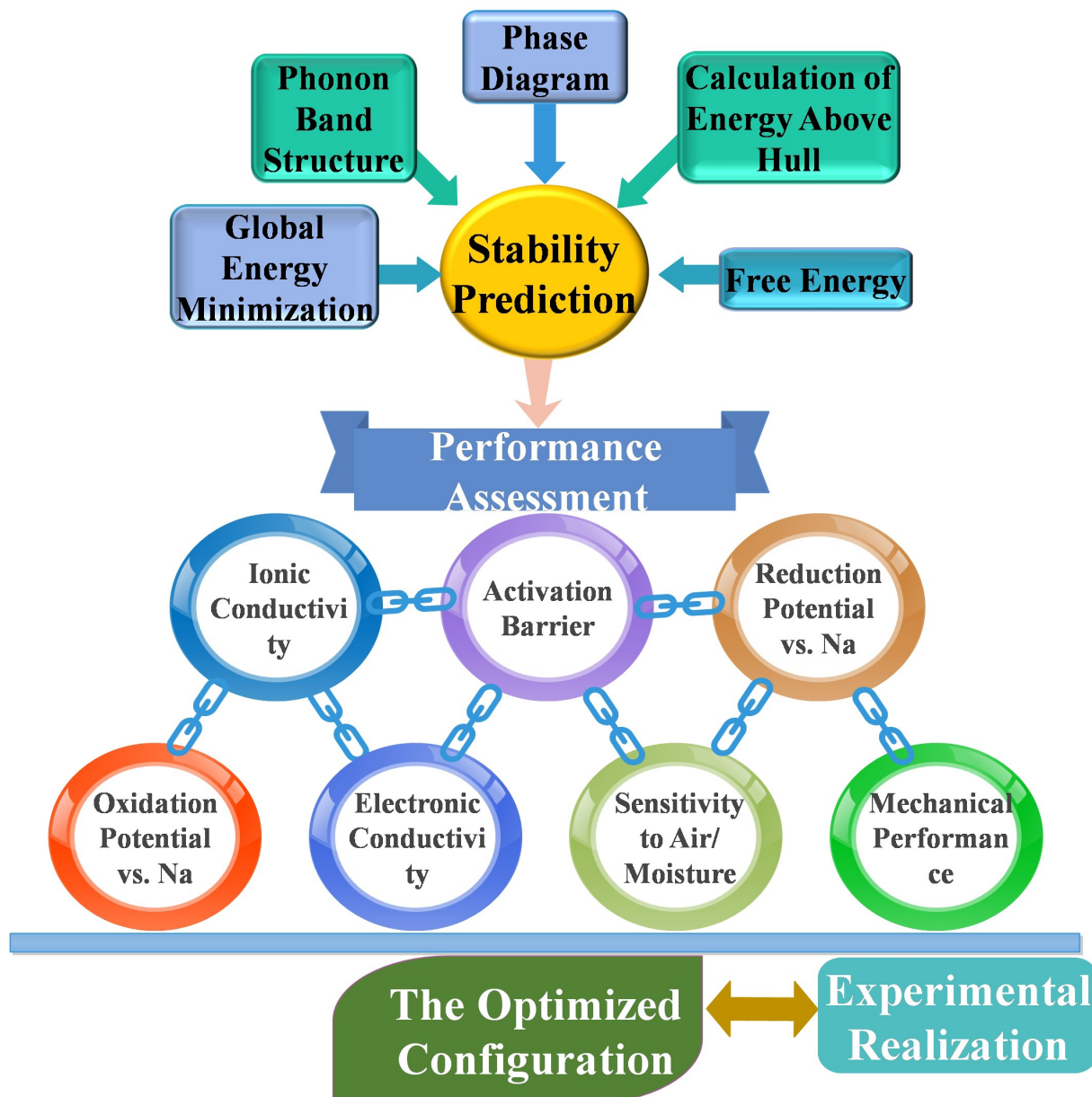


Special
Collection

Transport of Sodium Ions in Solids: Progress in First-Principle Theoretical Formulation of Potential Solid Sodium-Ion Electrolytes

Yuran Yu⁺^[a, b, c] Hongjie Xu⁺^[a, b, c] Zhuo Wang,^{*[a, b, c]} and Guosheng Shao^{*[a, b, c]}



All-solid-state sodium ion batteries (ASSIBs) have attracted great attention due to ever-increasing safety concern about current lithium ion batteries and the limited natural reserves of lithium. A major materials basis to enable high-performance ASSIBs lies in delivering ultra-fast Na^+ conductors, which is yet even more challenging than developing solid electrolytes for the lithium-ion batteries. This is largely attributed to limited fundamental understanding of the transportation characteristics of sodium

ions, which is rather different from the smaller alkali lithium ions. Here, we have carried out a perspective review of recent advances in theoretical formulation of novel solid electrolytes, focusing on methods, achievements, and the potential and shortcomings of identified materials systems. Efforts are made in offering a dependable framework to formulate fundamentally competitive materials to support developing "better" solid sodium-ion batteries.

1. Introduction

Lithium-ion batteries (LIBs) have been widely used to provide power for portable electronic devices and electric vehicles, and as well as for large-scale static energy storage, since they are able to store high densities of energy with a dependable technological basis.^[1–4] Global reserves of lithium are, however, rather limited, so that it is rather difficult to meet the steadily growing demand for energy storage.^[5] It is therefore necessary to develop alternative batteries based on more sustainable resources beyond LIBs.^[6–11] Among various alternative technologies, sodium ion battery (SIBs) is most attractive, since sodium with its almost unlimited resource is much cheaper than lithium.^[2,5] Even though SIBs are not so competitive as LIBs in terms of energy densities,^[6,12] they are highly advantageous for large scale energy storage. On the other hand, since sodium is chemically more reactive than lithium, there is even greater safety concern for SIBs^[13,14] and, similar to the LIBs, development of solid electrolytes based on inorganic compounds is considered to be a fundamental approach to mitigate the safety issues from use of flammable liquid organic electrolytes.^[15–17]

While remarkable achievements have been made in realization of high-performance solid-state lithium electrolytes (Li-SSE) to enable all solid lithium-ion batteries,^[18–24] the practical progress in developing solid electrolytes for sodium ion batteries (Na-SSE) has been rather struggling. This is largely attributable to the significantly larger and heavier sodium ions than lithium ones, in that the Na^+ radius (1.02 Å) is more than one-third larger than that of Li^+ (0.76 Å) and the atomic mass

of Na is over three times of that of Li (23 g mol⁻¹ of Na vs. 6.9 g mol⁻¹ of Li).^[12] In addition, the standard electrode potential of sodium is higher than that of lithium, being 2.71 V vs. 3.05 V below the standard hydrogen electrode (SHE).^[6] Such fundamental differences between the two alkali ions make it extremely difficult to mirror the success in developing Li-SSEs to Na-SSEs, so that straightforward copying Li-SSE success for SIB applications would be nearly impossible.

The main requests for promising Na-SSE include high ionic conductivity above 1 mS cm⁻¹, good chemical and electrochemical stability, insulating to electrons to avoid self-discharging and insensitive to ambient air and humidity, having a broad working temperature range encompassing the room temperature (RT) and good mechanical/processing properties, and being light, economical, and environmentally friendly.^[4,25–27] To date, the most studied inorganic Na-SSEs are still limited to materials based on the β -type Na-alumina (BASE), NASICON, sulfides, and anti-perovskites, as is summarized in Table 1.

The beta-type Na-alumina has been extensively investigated as ion conductor for electrochemical devices since its discovery in 1967.^[28,29] The beta alumina has two crystal structures, $\beta\text{-Na}_2\text{O}\cdot11\text{Al}_2\text{O}_3$ ($\text{NaAl}_{11}\text{O}_{17}$) and $\beta''\text{-Na}_2\text{O}\cdot5\text{Al}_2\text{O}_3$ (NaAl_5O_9).^[30,31] In the former phase of β -Na-alumina, there is only one mobile Na^+ within more than 5 alumina formula, leading to a poorer Na^+ conductivity of 1.2 mS cm⁻¹ in polycrystalline materials.^[29,32] In comparison, with the nearly doubled Na^+ content in the β'' -alumina, the ionic conductivity in polycrystalline β'' -Na-alumina is almost twice of that in the β phase, being 2 mS cm⁻¹ at room temperature.^[33] One notices that there exist huge gaps between the ionic conductivities in the single crystal and polycrystalline β'' -alumina materials. The main shortcomings of this materials system are high moisture sensitivity and poor mechanical strength and deformability, which are yet considered as main huddles against dependable processing and hence practical large-scale utilization.^[34]

NASICON on the basis of $\text{Na}_3\text{Zr}_2\text{Si}_2\text{PO}_{12}$ is another Na-SSE that has attracted considerable attention.^[35–37] The representative NASICON composition is a solid solution of $\text{Na}_3\text{Zr}_2\text{P}_3\text{O}_{12}$ by partial substitution of P by Si to form the series of $\text{Na}_{1+x}\text{Zr}_2\text{Si}_x\text{P}_{3-x}\text{O}_{12}$ ($0 \leq x \leq 3$) alloys.^[36,38] Through tuning the crystallite size and chemical composition at the boundaries, its particle or grain boundary resistance could be reduced. However, the reported ionic conductivity is yet inadequate in terms of practical request, and its poor deformability makes it difficult in realizing dependable solid batteries.^[39] Also, the reported solid-state synthesis method is very energy-consum-

[a] Y. Yu,[†] H. Xu,[†] Dr. Z. Wang, Prof. G. Shao
School of Materials Science and Engineering
Zhengzhou University
100 Kexue Avenue, Zhengzhou 450001, China
E-mail: wangzh@zzu.edu.cn
gsshao@zzu.edu.cn

[b] Y. Yu,[†] H. Xu,[†] Dr. Z. Wang, Prof. G. Shao
State Center for International Cooperation on Designer Low-Carbon &
Environmental Materials (CDLCEM)
Zhengzhou University
100 Kexue Avenue, Zhengzhou 450001, China

[c] Y. Yu,[†] H. Xu,[†] Dr. Z. Wang, Prof. G. Shao
Zhengzhou Materials Genome Institute
Building 2, Zhongyuanzhigu, Zhengzhou, Xingyang 450100, China

[†] These authors contributed equally to this work.

An invited contribution to a joint Special Collection between
ChemElectroChem and Batteries & Supercaps dedicated to research Beyond
Lithium-Ion Batteries.

Table 1. Summary of experimental performance of sodium ionic conductors.

Compounds	Ionic conductivity [mS cm ⁻¹]	Activation barrier [eV]	Grain boundary resistance [Ω]	Stable with O ₂ /moisture	Deformability
β-Na ₂ O·11Al ₂ O ₃ ^[32] (Single Crystal)	35	0.13	Non		
β-Na ₂ O·11Al ₂ O ₃ ^[32] (polycrystalline)	1.2	0.27 (25–200 °C)	large ^[26,31]		
β''-Na ₂ O·5Al ₂ O ₃ ^[29] (Single Crystal)	40	0.22 (25–200 °C)	Non	unstable ^[33]	bad ^[59]
β''-Na ₂ O·5Al ₂ O ₃ ^[28] (polycrystalline)	2	0.15–0.26	large ^[26,31]	unstable ^[33]	bad ^[59]
Na ₃ Zr ₂ Si ₂ PO ₁₂ ^[36]	0.67 ^[60,61]	0.353	120	stable	bad
Na ₁₀ SnP ₂ S ₁₂ ^[42]	0.4(RT)	0.356	370 (RT)	unstable	good
Na ₁₁ Sn ₂ P ₂ S ₁₂ ^[43]	1.4(RT)	0.25	760 (−20 °C)	unstable	good
Na ₃ OBr ^[49]	2.79×10 ^{−3} (110 °C)	0.68	22.3 K (110 °C)	unstable	
Na ₄ OI ₂ ^[62]	2.97×10 ^{−2} (180 °C)	0.646	2.4 K (180 °C)	unstable	

ing due to involvement of high-temperature sintering at above 1000 °C.^[36,38,39]

Sodium sulfide SSEs are considered as a promising class of Na⁺-SSEs owing to their higher Na⁺ conductivity than that of the NASICON alloys.^[26,40–44] Na₁₁Sn₂PS₁₂ is one of the best sulfide SSEs, whose development was largely inspired by the LGPS based lithium electrolytes.^[43,45] It demonstrated bigger Na⁺ conductivity than most oxides, experimentally confirmed to be up to 1.4 mS cm⁻¹ at room temperature together with a reasonably good activation energy of 0.25 eV. Besides, sodium sulfide SSEs are soft and highly deformable, which is highly helpful for cheaper processing based on cold-pressing to achieve fair grain/particle boundary quality. Also, the synthesis temperatures for sulfides are usually below 500 °C, being radically lower than those for oxide SSEs. Being similar to the

LGPS sulfides for solid LIBs, the main shortcoming of sulfide-based Na⁺ SSEs is their poor electrochemical compatibility with both high voltage cathodes and Na anode,^[46,47] and they are usually highly sensitive to humid air.^[48]

Cubic anti-perovskites (AP) such as Na₃OX (X = halogen) has also attracted a lot of attentions owing to their good compatibility with Na anode.^[25,49–52] Intriguingly, over the course of theoretical formulation for competitive Na-SSEs, a layer-structured Na₄OI₂ compound was identified as a stable phase at room temperature.^[51] Such a layered phase also belongs to the anti-perovskite class of Na-SSEs, which is able to accommodate plenty of Na⁺ ions up to 57 at.% in its unit cell. However, experimental exploitation of such Na-SSEs based on anti-perovskites (Na-AP) has yet been rather scarce. It was noted that serious particle boundary issues were experienced in cold-



Yuran Yu Received her Master degree in Department of Materials Science and Engineering from Zhengzhou University in 2020. Now she is working as a doctoral student in Prof. Shao's group in Zhengzhou University. Her research interests focus on materials genome method and all-solid-state batteries.



Hongjie Xu received her Master degree in Department of Materials Science and Engineering from Zhengzhou University in 2017. At that time, she is currently pursuing her PHD degree at Zhengzhou University. Her major research interests focus on all-solid-state lithium batteries and material genome method.



Zhuo Wang earned his PHD and graduated from theoretical physics department of Wuhan University, worked as a Lecturer in the physics department of Hubei University, and, in September 2017, joined in School of Materials Science and Engineering, Zhengzhou University, Professor Guosheng Shao's group, as Associate Professor. His research interests including, material genome method, all-solid-state battery, solar cell, sensor, metal ionic battery, and interfacial engineering.



Guosheng Shao is the Director of the State Centre for International Cooperation on Designer Low-carbon and Environmental Materials (CDLCEM) at the Zhengzhou University, China. He is also the Founding Director of the Zhengzhou Materials Genome Institute (ZMGI, 2016-) and Visiting Professor to the University of Surrey, UK (2018-). He earned his PhD in materials science at the University of Surrey and worked across UK universities as senior academic. His interest is “designer” materials and application devices, covering multiscale material modeling, advanced materials characterization and processing. His current focus is on sustainable (renewable) energy systems and environmental technologies.

processing their lithium ion counterparts (Li-APs), due to their brittleness and thus poor deformability. Recently, some practical strategies, such as amorphization^[53,54] or mixing/wetting with liquid organic electrolyte,^[55] have been demonstrated to help reduce the boundary problems in anti-perovskite Li-APs.

It has been recognized that fundamental understanding is essential for cost-effective development of novel materials when there is limited practical knowledge. This is particularly true for developing solid battery materials beyond the LIB technologies such as solid SIBs, when initial efforts to extend the Li-SSE systems into Na-SSEs have been miserably unsuccessful. Encouragingly, significant advances have been made in establishing first principle frameworks towards formulating solid battery materials, so that a fundamental basis can be established in the spirit of Materials Genome Initiative or materials informatics, which relies on fundamental materials information to predict potential new formulae towards quickened experimental exploitation.^[56–58] Here in this work, we have carried out a perspective review of the recent advances in theoretical modeling of solid sodium ion conductors, aiming to outline fundamental insights to guide DFT formulation of novel electrolytes for solid sodium ion batteries. We start with outlining the theoretical framework on the basis of the current state of the arts, followed by reviewing modeling achievements in various systems. Efforts are made to shed lights on principles as effective guidance for alloy development.

2. DFT-Based Material Formulation Approach

A summary of the current DFT methods leads to an integrated first-principles material formulation approach, as shown in Figure 1. This covers both materials stability and functional properties.

The stability task starts at identifying thermodynamically stable structure for each composition, through extensive global energy minimization covering a composition-structure space without consideration of thermal contribution, thus resulting in an energy convex hull with respect to composition change. The dynamic stabilities of these identified structures will be checked and the resultant phonon entropy will then be utilized to construct the free energies for the assessment of phase stability at elevated temperatures. Each structure on or close to the energy convex hull will then be subject to energetic checking against that of stable constituent phases, in order to check whether the phase is truly stable against the equilibrium energy hull. The most stable phase for each composition can be readily identified using a global energy minimizer such as the universal structure predictor (USPEX).^[63,64] The dynamic stability of each low-energy phase can be assessed on the basis of phonon band structures.^[65,66]

Stable constituent phases are to be identified either by extensive calculations or from available databases, e.g. by consulting phase diagram handbooks, thermodynamic databases combined with the established calculation-of-phase-diagram (CALPHAD) method,^[67] or the databank in the Materials

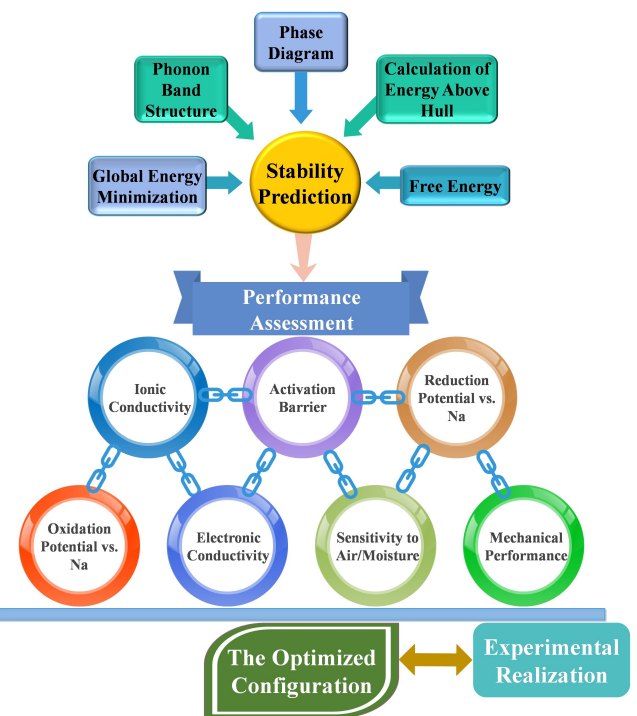


Figure 1. DFT framework for material formulation.

Project webpage (<https://www.materialsproject.org>).^[68,69] Such stable constituent phases are considered for the calculation of the energy above the equilibrium energy hull, so that phases with total energy below the hull have no tendency to decompose. Free energies for each dynamically stable phase can be formulated with the consideration of the phonon entropy.^[70]

Phases satisfying these stability criteria will then be subject to assessment of properties/functionalities, which covers ionic diffusion, ionic conductivity, electrochemical potential, electronic band structure, electrochemical stability against electrodes, elastic tensors, sensitivity to ambient atmosphere (air, moisture) etc. The fundamental basis for dependable DFT assessment of electrochemical and transport properties lies in their being largely dictated by the cohesive energy with reference to free atoms in vacuum when non-local contribution to the exchange-correlation (XC) functionals is trivial. A more detailed discussion on XC functionals is presented in a recent paper.^[58]

The ionic conductivity is determined by diffusion of the alkali ions, usually following an Arrhenius relationship, $D = D_0 \exp\left(-\frac{E_a}{k_B T}\right)$, with D_0 being a constant, E_a the activation energy, and k_B the Boltzmann constant. Both *ab initio* molecular dynamics (AIMD)^[74–77] and the *climb image nudged elastic band* (CI-NEB)^[71–73] have been employed to characterize the diffusion characteristics of alkali ions. It is also necessary to carry out AIMD at elevated temperature for dependable AIMD simulation, as the steady state cannot be reached otherwise within the tractable duration for DFT calculation.^[9,58]

While the CI-NEB method,^[78] has been shown to be a useful means in identifying diffusion pathways and associated

activation energies,^[9,51,66,74] the recently established AIMD method is considered to be a more powerful tool owing to its capability in establishing the complete diffusion expression using the resultant mean square displacement (MSD)^[9,25,50,56,71,79] at each temperature T over a period of time (t), $\langle [\Delta r(t)]^2 \rangle$ [Eq. (1)]:

$$D = \frac{1}{2dt} \langle [\Delta r(t)]^2 \rangle \quad (1)$$

as long as the trajectories are “unwrapped” to correct artefacts due to use of small systems necessary for feasible DFT simulation.^[73] It is necessary to carry out AIMD at elevated temperature for dependable simulation, as steady state cannot be reached otherwise within the practical temporal duration for DFT calculation.^[9,58,72] Notably, AIMD simulations should be carried out over a reasonable timescale with sufficient number of atoms, in order to cover adequate events to safeguard reliability.^[80] The activation energies from AIMD and CI-NEB are often in good agreement, when the CI-NEB pathways are dominant in the statistic process typical over a molecular dynamic process. It has been revealed, however, complex pathways with coordinated diffusion modes out of the static CI-NEB may not be significant in the dynamic AIMD processes.^[9,71,78]

The ionic conductivity σ is related to diffusion data by the Nernst – Einstein equation [Eq. (2)]^[79,81]

$$\sigma = \frac{\rho z^2 F^2}{RT} D = \frac{\rho z^2 F^2}{RT} D_0 \exp\left(-\frac{E_a}{k_B T}\right) \quad (2)$$

where ρ is the molar density of diffusing alkali ions in the unit cell, z is the charge per alkali ion (+1 for Na^+), F and R are the Faraday's and the gas constants, respectively.

The electronic band structure needs to be calculated to make sure that the bandgap of each identified electrolyte is sufficiently large to avoid considerable electronic conductivity. Non-local contribution to exchange functionals usually needs to be considered for the prediction of the bandgaps, e.g. using hybrid functionals, such as the HSE06.^[82–84]

The change of configurational energy for a Na-SSE against Na content, x , can be readily established, e.g. using the Alloy-Theoretic Automated Toolkit (ATAT) for energy minimization through the composition-configuration space between two terminal compositions.^[85,86] The average electrochemical potential between state A ($\text{Na}_x \prod$) and state B ($\text{Na}_{x+\Delta x} \prod$), $\bar{V}_{A \rightarrow B}$, vs. that of the pure Na anode, is related to the total energies (E_{total}) as [Eq. (3)]:^[79,87]

$$\bar{V}_{A \rightarrow B} = -1/z \{ [E_{\text{total}}(A_{x+\Delta x} \prod) - E_{\text{total}}(A_x \prod)] / \Delta x - E_{\text{total}}(A) \} \quad (3)$$

where x is the number of Na^+ in the formula unit of $\text{Na}_x \prod$, charge value $z=1$ for sodium ion, Δx is the change in the sodium content, and \prod is the collection of other elements.

Mechanical properties also need to be evaluated through calculated elastic tensor C_{ij} , so that bulk (B), shear (G) and Young's (E) modulus and Poisson's ratio (ν) can be derived from the Voigt–Reuss–Hill (VRH) approximation.^[88–90] The Young's moduli E and Poisson's ratios ν are related to the bulk and shear moduli B and G as [Eqs. (4), (5)]

$$E = \frac{9BG}{(3B+G)} \quad (4)$$

$$\nu = \frac{(3B-2G)}{2(3B+G)} \quad (5)$$

The latter is an effective indicator on plastic deformability, with smaller B/G ratio leading to larger ν to benefit plasticity.

3. Transportation of Na^+ in Inorganic Solid-State Electrolytes

3.1. $\text{Na}-\beta/\beta''\text{-Alumina (BASE)}$

Even though the BASE system of solid electrolyte was discovered for over a half century, achievements so far were largely on experimental efforts towards synthesis and properties. Figure 2 shows the $\text{Na}-\beta/\beta''\text{-alumina}$ structures, i.e. $\beta\text{-Na}_2\text{O}\cdot11\text{Al}_2\text{O}_3$ ($\text{NaAl}_{11}\text{O}_{17}$) and $\beta''\text{-Na}_2\text{O}\cdot5\text{Al}_2\text{O}_3$ (NaAl_5O_8).^[28,30,31] The β structure is hexagonal with a $P6_3/mmc$ space group, and the β'' phase has a rhombohedral structure of $\bar{R}\bar{3}m$. Both phases are constructed by the AlO_4 tetrahedral and AlO_6 octahedral units in quite a similar way, with different levels of Na contents leading to changed crystal symmetry. In the conduction planes for Na^+ , two AlO_4 tetrahedral units sharing one atomic O to prop up a two-dimensional channel for Na^+ diffusion. The main difference between $\text{Na}-\beta\text{-alumina}$ and $\text{Na}-\beta''\text{-alumina}$ lies in the concentration of Na^+ ions in the diffusion channel. The Na^+ content in the latter is about twice of that in the former, leading to weaker electrostatic attraction from the bridging oxygen ions and a larger room-temperature Na^+

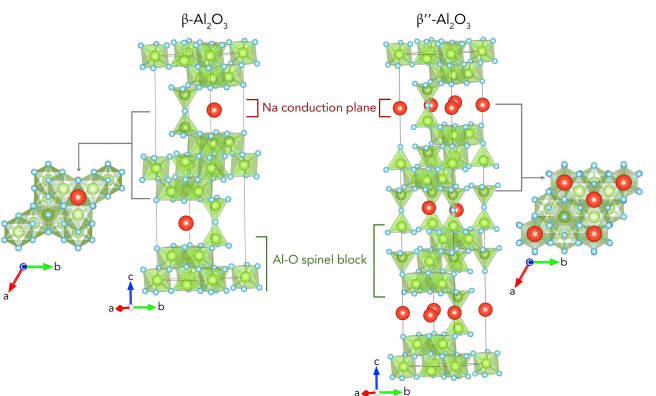


Figure 2. Crystal Structures of $\text{Na}^+-\beta\text{-alumina}$ and $\text{Na}^+-\beta''\text{-alumina}$. Reproduced from Ref. [26] with permission. Copyright (2018) Elsevier.

conductivity about 2 mS cm^{-1} . However, materials based solely on the β'' phase is not desirable, due to its poor mechanical performance and high sensitivity to humidity.^[31] Suitable mixing of the two phases with stabilizing alloying were shown to be useful for improved properties. Systematic fundamental modeling is yet desired to shed further light upon the enormous “grain boundary” resistances, since surfaces and grain boundaries are typically recognized as fast diffusion paths in condensed matter. It has been shown recently that grain boundaries are not necessarily an issue once the bulk ionic conductivity was adequately high.^[56]

3.2. NASICON-Type SSE Based on $\text{Na}_3\text{Zr}_2\text{Si}_2\text{PO}_{12}$

NASICON materials contain three-dimensional (3D) as fast channels for Na^+ migration.^[91,92] Most efforts on NASICON were on the basis of $\text{Na}_3\text{Zr}_2\text{Si}_2\text{PO}_{12}$ owing to its better ionic conductivity.^[92] As shown in Figure 3,^[36] $\text{Na}_3\text{Zr}_2\text{Si}_2\text{PO}_{12}$ can exist in two different phases, either rhombohedral ($\bar{\text{R}}3\text{c}$) or monoclinic ($\text{C}2/\text{c}$). They are made of corner-sharing SiO_4/PO_4 tetrahedra and ZrO_6 octahedra. The rhombohedral phase contains two Na^+ sites, while the monoclinic structure has three Na^+ sites in its lattice.

In the monoclinic $\text{Na}_3\text{Zr}_2\text{Si}_2\text{PO}_{12}$, five lattice sites are involved in the 3D diffusion of Na^+ .^[36] One can see from the Na^+ trajectory map over AIMD evolution at 1400 K, Figure 3(a)-(b), that a lower probability density for Na^+ ions appear between two adjacent bc -planes. The Na^+ probability density along the $\text{Na}2\text{-Na}5$ pathway is evidently lower than that in along the $\text{Na}3\text{-Na}4\text{-Na}5$, suggesting that the $\text{Na}2\text{-Na}5$ is not favorable due to higher activation barrier.

The corresponding Na^+ -ion probability density in rhombohedral $\text{Na}_3\text{Zr}_2\text{Si}_2\text{PO}_{12}$ at 1400 K is shown in Figure 3(c)-(d).^[33] Two proposed pathways, along $\text{Na}2\text{-Na}3\text{-Na}1\text{-Na}3\text{-Na}2$ or $\text{Na}2\text{-Na}3\text{-Na}3\text{-Na}2$ (Figure 3e), were identified. As is shown in Figure 3(d), no evident difference in the Na^+ probability density exists between the $\text{Na}2\text{-Na}3\text{-Na}1\text{-Na}3\text{-Na}2$ and $\text{Na}2\text{-Na}3\text{-Na}3\text{-Na}2$ pathways. It was also concluded that the $\text{Na}2\text{-Na}1\text{-Na}2$ pathway is more preferable than the direct $\text{Na}2\text{-Na}2$ pathway proposed by Tranqui.^[93]

CI-NEB calculations were then carried out to quantify the activation barriers in the monolithic phase.^[36] Single ion migration mechanisms were compared in the monoclinic phase, different Na^+ hopping pathways along the $[1\ 0\ 1]$ direction and in the bc -plane were investigated, Figure 3(e)-(g). The migration barriers along the $[1\ 0\ 1]$ direction and the two possible routes in the bc -plane are 0.392, 0.306, and 0.312 eV, correspondingly.

Possible correlated migration of Na^+ -ions along the above pathways were also studied. During the correlated hopping process, when a Na^+ jumps to its nearest vacant site, a vacancy site is left behind, which is then filled by an adjacent Na^+ . The activation barriers for such coordinated hopping of Na^+ ions are 0.338, 0.257, and 0.187 eV, correspondingly (Figure 3(h)-(j)). The activation barriers for coordinated hopping were shown to be considerably lower than those for independent hopping

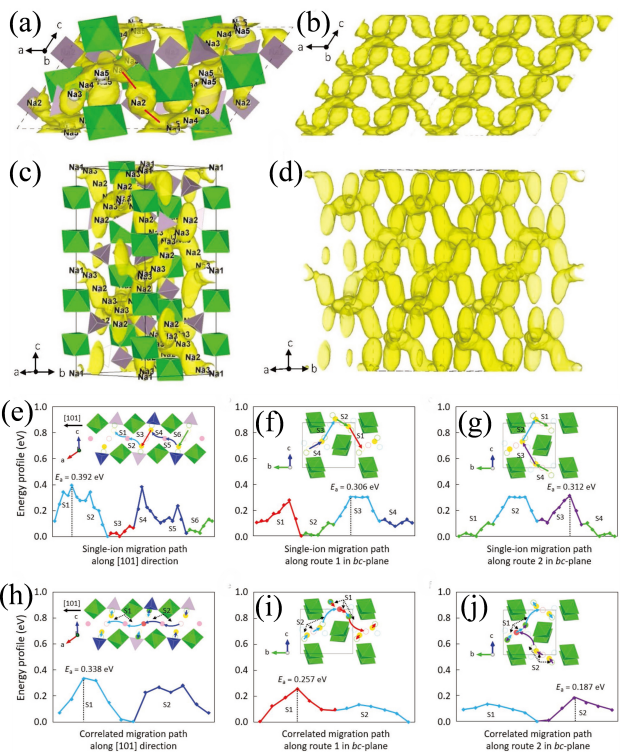


Figure 3. a, b) The Na-ion probability density isosurfaces (yellow) of monoclinic $\text{Na}_3\text{Zr}_2\text{Si}_2\text{PO}_{12}$ at 1400 K from AIMD simulation: The red lines in (a) indicate the $[101]$ direction, which is the rate-limiting step in the Na^+ -ion migration process. c, d) The Na^+ -ion probability density isosurface (yellow) of rhombohedral $\text{Na}_3\text{Zr}_2\text{Si}_2\text{PO}_{12}$ at 1400 K from AIMD simulations; all pathways follow the $\text{Na}2\text{-Na}3\text{-Na}1\text{-Na}3\text{-Na}2$ trajectory, and no $\text{Na}2\text{-Na}2$ diffusion is observed. Energy barriers for single-ion migration and correlated migration mechanism from CI-NEB. Energy profile and schematic diagram of single ion migration and multi-ion correlated migration in monoclinic $\text{Na}_3\text{Zr}_2\text{Si}_2\text{PO}_{12}$. e-g) The energy barrier of a single Na-ion along $[101]$ direction, route 1 in bc -plane, and route 2 in bc -plane. h-j) The energy barrier along $[101]$ direction, route 1 in bc -plane, and route 2 in bc -plane for correlated migration of multiple Na-ions. $\text{Na}1$ sites (4d) are rose spheres, $\text{Na}2$ sites (4e) are pink, $\text{Na}3$ sites (8f) are green, $\text{Na}4$ sites (8f) are gold, and $\text{Na}5$ (8f) are turquoise. The spheres denote the sites which are occupied in the initial structure, while the circles denote the sites which are unoccupied. Reproduced from Ref. [36] with permission. Copyright (2019) Wiley-VCH.

processes. As the diffusion coefficient has not been quantified, it is yet inconclusive about the contribution of the different CI-NEB mechanisms to the overall ion transportation. AIMD quantification of both diffusion coefficient and ionic conductivity would be highly useful, so that the effective activation barrier can be derived with the dictating mechanisms being identified.^[9,71,78] The activation barrier along the $[1\ 0\ 1]$ direction in the monolithic phase is considerably larger than those within the bc -planes, making diffusion in this direction particularly problematic.

3.3. Sulfide-Based Electrolyte $\text{Na}_{11}\text{Sn}_2\text{PS}_{12}$

The milestone experimental discovery of $\text{Li}_{10}\text{GeP}_2\text{S}_{12}$ (LGPS) showed for the first time that the ionic conductivity of a solid-state Li^+ electrolyte can beat that of liquid organic electrolytes

with remarkable Li^+ conductivity over 10 mS cm^{-1} at room temperature.^[20] However, a straightforward substitution of Li with Na in proven Li-SSEs was not successful. The $\text{Na}_{10}\text{MP}_2\text{S}_{12}$ (NGPS with M=Ge, Si, Sn) was such an attempt to copy the success of LGPS to NGPS. Even though the two systems have the same structural type (P_4/nmc , Figure 4(a)-(b)),^[42] Diffusion of Na^+ in the NGPS is much more difficult than Li^+ in the LGPS, even though DFT calculations revealed the same preferred ion diffusion channel along the c-axis as in LGPS (Figure 4(c)). The activation barrier for Na^+ in $\text{Na}_{10}\text{SnP}_2\text{S}_{12}$ is much higher (0.317 eV vs. 0.25 eV for Li^+ in LGPS), and experimental studies showed that the activation barrier for Na^+ transport was slightly higher than the theoretical value for single crystal, being 0.356 eV, with an ionic conductivity only 0.4 mS cm^{-1} at room temperature.

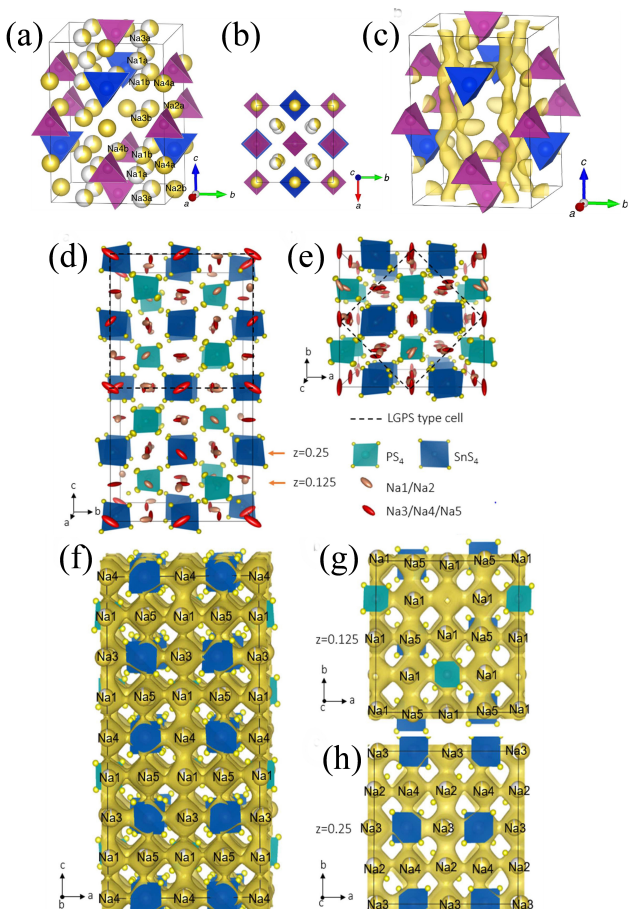


Figure 4. a, b) Structure of $\text{Na}_{10}\text{SnP}_2\text{S}_{12}$ from DFT calculations. c) Na -ion probability density isosurface (yellow) of $\text{Na}_{10}\text{SnP}_2\text{S}_{12}$ from 600 K AIMD simulation. SnS_4 tetrahedra are marked in blue, PS_4 tetrahedra in purple. Reproduced from Ref. [42] with permission. Copyright (2016) The Authors. d) Structure of $\text{Na}_{11}\text{Sn}_2\text{PS}_{12}$ from single crystal data. The framework showing ordering of the SnS_4 (dark blue) and PS_4 (light blue) tetrahedra; yellow spheres are S; and rose/red ellipsoids are sodium ions. e) The small tetragonal cell of $\text{Na}_{11}\text{Sn}_2\text{PS}_{12}$; f) Na -ion probability density isosurface (yellow) obtained from AIMD studies at 1050 K for 40 ps, the sodium diffusion along the c axis involves a pathway along -Na(4)-Na(1)-Na(3)-Na(1)-chains; the Na -ion probability density obtained from the AIMD Na -ion trajectories in the ab plane shows the pathways at g) $z=0.125$ and h) $z=0.25$. Reproduced from Ref. [43] with permission. Copyright (2017) Royal Society of Chemistry.

Later, by using excess Na off the $\text{Na}_{11}\text{Sn}_2\text{PS}_{12}$ stoichiometry, a different phase of tetragonal space group I4/acd was synthesized.^[43] It was revealed that the Na^+ transport channels followed a pathway linking 3D face-sharing octahedral sites in the $\text{Na}_{11}\text{Sn}_2\text{PS}_{12}$ phase, as shown in Figure 4(f)-(h). The unique structure with ordered Sn/P tetrahedral arrangement led to significant enhancement of ionic conductivity in $\text{Na}_{11}\text{Sn}_2\text{PS}_{12}$, with the activation barrier being reduced down to 0.25 eV and ionic conductivity being increased up to 1.4 mS cm^{-1} at room temperature.^[43]

Also, being similar to the LGPS for LIBs, $\text{Na}_{11}\text{Sn}_2\text{PS}_{12}$ was also found to be incompatible with the alkali Na anode due to tendency of interfacial reaction.^[47] The calculated SSE stability window vs. Na is only 0.57 V (from 1.25 to 1.82 V), which is insufficient to prevent the formation of electrolyte-electrode interphase, either below 1.25 V with the Na anode or above 1.82 V with the cathode.^[47]

3.4. Anti-Perovskites

3.4.1. Hali-Chalcogenides

The Goldschmidt tolerance factor, $t = (R_{\text{Na}} + R_X)/\sqrt{2}$, is indicative of the stability of an anti-perovskite phase Na_3AX ($\text{A}=\text{chalcogen}$, $\text{X}=\text{halogen}$), with t from 0.8 to 1 to favor an anti-perovskite structure.^[94–96] An anti-perovskite structure is constructed by Na_6O with halogen X site sitting at the octahedral center, Figure 5(a).^[49] However, the NEB data for Na_3OX based on the vacancy mechanism predicts rather high activation

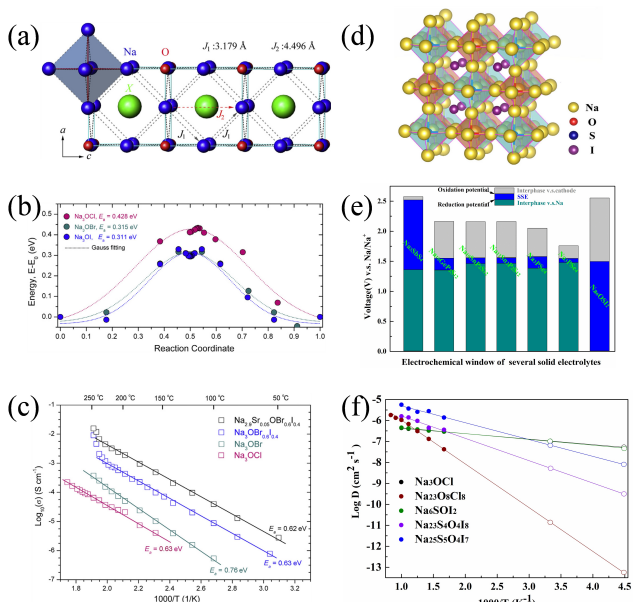


Figure 5. a) The crystal structure, b) Energy for sodium migration, and c) Arrhenius plots of $\log(D)$ versus $1/T$ of the anti-perovskites Na_3OX ($\text{X}=\text{Cl}, \text{Br}, \text{I}$). Reproduced from Ref. [49] with permission. Copyright (2015) Elsevier. d) The crystal structure, e) oxidation potential and reduction potential, and f) diffusion coefficients for sodium ions from AIMD simulation of double-anti-perovskite structural. Reproduced from Ref. [25] with permission. Copyright (2018) Royal Society of Chemistry.

barriers E_a in the range from 0.311 to 0.428 eV, Figure 5(b). The experimentally achieved activation barriers in polycrystalline materials were nearly twice of the theoretical values, with the associated ionic conductivities being only in the order of 10^{-3} mS cm $^{-1}$, Figure 5(c).

Through lattice softening with alternating occupancy of the A site by O and S and the X site being occupied by I (Figure 5(d)), the most stable phase turns into a new structure with a double-anti-perovskite symmetry at a stoichiometry of Na₆SOI₂.^[25] The dictating diffusion pathway is along the connected edges of chalcogen-centered octahedrons, so that the electrostatic interaction between the central chalcogen anion and the Na $^+$ cation is the main origin of diffusion barrier. The incorporation of S lowers the electrostatic interaction between sodium and the chalcogen ions, thus promoting the ionic conductivity. The use of a bigger halogen I helps to prop up a bigger lattice and thus reduce overall binding. Furthermore, slight off-stoichiometry, with Na enrichment and chalcogen substitution of halogen to maintain charge neutrality, leads to significantly reduced activation barrier and enhanced ionic conductivity. This is attributed to the presence of interstitial Na $^+$ in the structure, which leads to shortened hopping distance and weakened electrostatic interaction with the chalcogen anions, owing to charge screening from neighbor alkali cations. The ionic conductivity of Na₂₅S₅O₄I₇ is predicted to be as high as 10.36 mS cm $^{-1}$ at room temperature and the low activation energy of only 0.16 eV is key to permit a quite high ionic conductivity of 1.79 mS cm $^{-1}$ at -50°C , as shown in Figure 5(f). Besides, this theoretically identified solid electrolyte is electrochemically compatible with Na anodes (Figure 5(e)), with a wide energy gap to prevent conduction of electrons.

It is noted that similar to most reported SSEs based on sulfides or hali-sulfides, the double anti-perovskite Na₆SOI₂ phase is slightly metastable with respect to the stable constituents. There is hence a fundamental tendency for its decomposition into the stable ground-state constituents of Na₄OI₂ and Na₂S. The stable Na₄OI₂ phase has a layered structure with arrangement of Na₆A octahedrons being in a similar way to that in the anti-perovskite in each layer.^[51] Naturally, the extension of the alloying chemistry concepts from the aforementioned three-dimensional Na₆SOI₂ phase leads to the theoretical identification of the layered double-anti-perovskite, which is a stable Ruddlesden–Popper type double anti-perovskite, with the stoichiometry of Na₄S_{0.5}O_{0.5}I₂. Furthermore, ATAT simulation predicts that iso-valent replacement of Na with Li, over Na_{4(1-x)}Li_xS_{0.5}O_{0.5}I₂ ($0 \leq x \leq 1$), is thermodynamically allowed, with the minimum on the energy convex hull corresponding to a quarter substitution of Na by Li. It is amazing that such a Na₃LiS_{0.5}O_{0.5}I₂ phase is stable both thermodynamically and dynamically. The predicted activation barrier for Na $^+$ diffusion in Na₃LiS_{0.5}O_{0.5}I₂ is as low as 0.12 eV, with a remarkable Na $^+$ conductivity as high as 6.3 mS cm $^{-1}$. Such low activation energy is only about half of the Li $^+$ activation in the LGPS system, which safeguards outstanding ionic conductivity beyond 1 mS cm $^{-1}$ even at -50°C as demonstrated in Figure 6(d). The co-existence of smaller Li $^+$

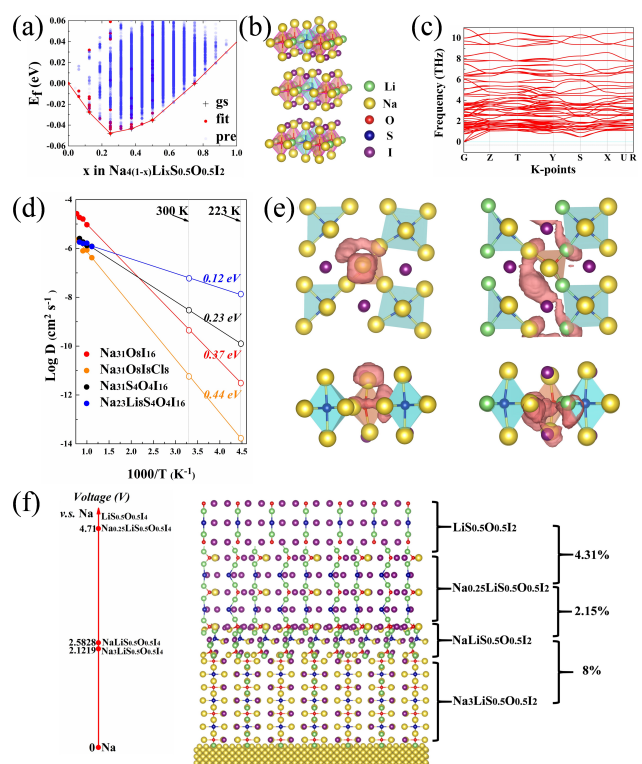


Figure 6. a) The convex hull for Na_{4(1-x)}Li_xS_{0.5}O_{0.5}I₂ ($0 \leq x \leq 1$) through ATAT simulation. b) Stable structure for Na₃LiS_{0.5}O_{0.5}I₂.65 corresponding to minimal energy. c) Calculated phonon band structures for Na₃LiS_{0.5}O_{0.5}I₂. d) Diffusion coefficients for sodium ions from AIMD simulation. e) Projections of diffusion trajectories of sodium ions from the top and side view for Na₃S₄O₄I₁₆ (left) and Na₂₃Li₈S₄O₄I₁₆ (right), over a simulation time of 90 ps at 800 K. f) Electrochemical potentials for ground-state stable structures of Na_{3(1-y)}Li_{1-x}S_{0.5}O_{0.5}I₂ ($0 \leq x, y \leq 1$) from ATAT simulation and the percentages on the right refer to lattice mismatches. Reproduced from Ref. [51] with permission. Copyright (2019) The Authors.

ions at the Na $^+$ lattice sites leads to a knocking-on effect, which helps the hopping of the bigger and heavier Na $^+$ ions. The overall Na $^+$ /Li $^+$ ion trajectories for Na₃LiS_{0.5}O_{0.5}I₂ are shown in Figure 6(e), where planar highways for the diffusion of alkali ions exist between the layered structural units.

It is also found that depletion of Na $^+$ enhances the oxidation potential of the Na_{3(1-y)}Li_{1-x}S_{0.5}O_{0.5}I₂ ($0 \leq x, y \leq 1$). The predicted stable structures with corresponding electrochemical windows are shown in Figure 6(f). It is highly encouraging that the lattice mismatches between neighboring Na-depletion configurations are rather limited below 8%.^[51] Fundamentally, this material system is able to provide a series of stable phases to function as a high voltage/capacity cathode, superb electrolyte and artificial cathode interphase layer.

3.4.2. Hali-Sulfates

The sodium hali-sulfate Na₃(SO₄)F_{0.5}Cl_{0.5} compound is a natural mineral, which was recognized for its light-emitting functionality. Figure 7(a) shows the structural configuration of Na₃SO₄F_{0.5}Cl_{0.5}, which is constructed by alternating arrangement

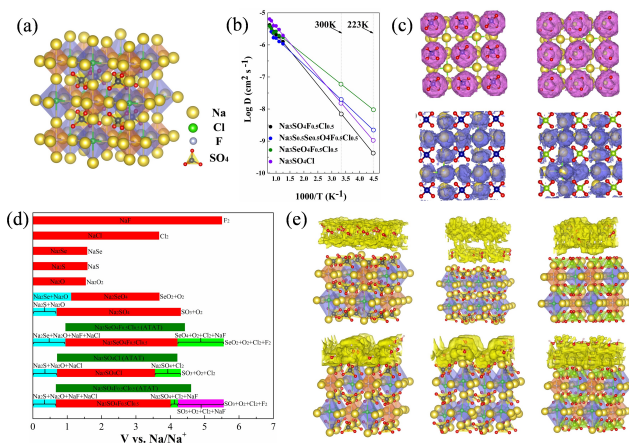


Figure 7. a) The configurations of $\text{Na}_3\text{SO}_4\text{F}_{0.5}\text{Cl}_{0.5}$; b) diffusion coefficients for sodium ions obtained from AIMD simulation; c) diffusion trajectories of oxygen and sodium ions in $\text{Na}_3\text{SO}_4\text{F}_{0.5}\text{Cl}_{0.5}$ and $\text{Na}_3\text{SeO}_4\text{F}_{0.5}\text{Cl}_{0.5}$ over a simulation time of 180 ps at 1000 K; d) plot of Na uptake per formula unit of solid electrolyte (red solid) against voltage vs. Na/Na^+ ; e) AIMD simulation to reveal the interaction of oxygen and water, showing trajectories of O_2^- (top) and H^+ (bottom) next to $\text{Na}_3\text{SO}_4\text{F}_{0.5}\text{Cl}_{0.5}$, $\text{Na}_3\text{SO}_4\text{Cl}$ and $\text{Na}_3\text{SeO}_4\text{F}_{0.5}\text{Cl}_{0.5}$ (from left to right) over a simulation time of 180 ps at 300 K. Reproduced from Ref. [52] with permission. Copyright (2019) Royal Society of Chemistry.

of halogen-centered octahedrons of Na_6F and Na_6Cl on the corners of a cubic lattice, with the SO_4^{2-} group sitting at the lattice center. This is another type of double-anti-perovskite phase, with alternating occupancy of the halogen site by F and Cl inducing a face-centered space group of $\text{Fm}\bar{3}\text{m}$ (225).^[52] Further tuning of the lattice chemistry on the chalcogen or halogen site leads to several stable phases with improved ionic conductivity, as is summarized in Figure 7(b). The predicted Na^+ conductivity in the pristine phase $\text{Na}_3\text{SO}_4\text{F}_{0.5}\text{Cl}_{0.5}$ is 1.086 mS cm^{-1} at 300 K with an activation barrier of 0.21 eV. When F is completely replaced by the bigger Cl, the ionic conductivity in $\text{Na}_3\text{SO}_4\text{Cl}$ enlarges to 2.328 mS cm^{-1} at 300 K owing to bigger halogen-Na spacing. When S in SO_4^{2-} at the lattice center is partially replaced by Se, the activation barrier in $\text{Na}_3\text{S}_{0.5}\text{Se}_{0.5}\text{O}_4\text{F}_{0.5}\text{Cl}_{0.5}$ lowers further to 0.163 eV and the ionic conductivity will be increased to 2.817 mS cm^{-1} at room temperature. Full substitution of S with Se reduces the activation energy down to 0.137 eV and increases the Na^+ conductivity up to 8.167 mS cm^{-1} (300 K) in $\text{Na}_3\text{SeO}_4\text{F}_{0.5}\text{Cl}_{0.5}$.

From examining the AIMD trajectories, one recognizes that the O_2^- anions in the SeO_4^{2-} group can shake/vibrate wildly around each hub Se/S, making each AO_4^{2-} clusters move like a wobbling “waterwheel”. Such wildly wobbling waterwheels will knock on neighboring sodium ions, thus sending them to hop away along the edges of $\text{Na}_6\text{Cl}/\text{Na}_6\text{F}$ octahedrons for highly enhanced long-range migration (Figure 7(c)). One can see the significant enhancement for ionic conductivity in $\text{Na}_3\text{SeO}_4\text{F}_{0.5}\text{Cl}_{0.5}$ above that in $\text{Na}_3\text{SO}_4\text{F}_{0.5}\text{Cl}_{0.5}$. It is the weaker Se–O than S–O binding that leads to the larger SeO_4^{2-} unit, which in turn exerts stronger knocking-on effects to Na^+ ions. Such knocking-on effect is analogous to installing a sub-nano-machine within each compound lattice, which functions to pump alkali ions like a water mill.

The calculated electrochemical windows for the identified phases are summarized in Figure 7(d). None of the $\text{Na}_3\text{SeO}_4\text{F}_{0.5}\text{Cl}_{0.5}$, $\text{Na}_3\text{SO}_4\text{F}_{0.5}\text{Cl}_{0.5}$ or $\text{Na}_3\text{SO}_4\text{Cl}$ are electrochemically stable against the Na anode due to potential reactions in between, so that protective coating would be needed to protect the alkali anode. In contrast, their oxidation potentials are quite high, well above 3.5 V, making them electrochemically stable against high voltage cathodes for SIBs. The maximum oxidation potential from an ATAT simulation with sodium depletion are understandably higher than the equilibrium limits when constituent phases are not considered.

AIMD simulation was carried out over electrolyte slabs with neighboring O_2 or H_2O , including $\text{O}_2|\text{Na}_3\text{SO}_4\text{F}_{0.5}\text{Cl}_{0.5}$, $\text{O}_2|\text{Na}_3\text{SO}_4\text{Cl}$, $\text{O}_2|\text{Na}_3\text{SeO}_4\text{F}_{0.5}\text{Cl}_{0.5}$, $\text{H}_2\text{O}|\text{Na}_3\text{SO}_4\text{F}_{0.5}\text{Cl}_{0.5}$, $\text{H}_2\text{O}|\text{Na}_3\text{SO}_4\text{Cl}$ and $\text{H}_2\text{O}|\text{Na}_3\text{SeO}_4\text{F}_{0.5}\text{Cl}_{0.5}$. The AIMD trajectories of H_2O or O_2 next to the (001) surface for each compound are presented in Figure 7(e), showing that the structural frameworks for these compounds are maintained without reaction with molecules of O_2 or H_2O , indicating good resilience of these potential SSEs against humid air.

Modeling results on Na-SSEs reviewed in this work are summarized in Table 2, covering methods used, ionic conductivity, activation energy, electrochemical windows and stability against humid air. The resultant data sets demonstrate that the latest identified configurations of hali-chalcogenides with double-anti-perovskite type of structures are remarkably attractive, on the basis of superb ionic conductivity, very low activation energy, improved stabilities to humidity and oxygen and remarkably wide electrochemical windows. It is worth

Table 2. Summary of modeling results from published work, covering methods and outcome.

Compounds	USPEX	Phonon	Free energy (at 0 K)	Gibbs free energy	Na ⁺ ionic conductivity (AIMD) [mS cm ⁻¹] RT	Na ⁺ ionic conductivity (AIMD) [mS cm ⁻¹] -50 °C	Activation barrier [eV] AIMD	Activation barrier [eV] CINEB	Voltage plateau [V]	Bandgap [eV]	Sensitivity to air/moisture
BASE	/	/	/	/	/	/	/	/	/	/	/
$\text{Na}_3\text{Zr}_2\text{Si}_2\text{PO}_12$	/	/	/	/	/	/	0.306–0.392 ^[36]	/	1.11–3.64 ^[99]	/	/
$\text{Na}_{10}\text{Sn}_2\text{P}_2\text{S}_12$ ^[42]	/	/	Yes	/	0.94	/	0.317	/	1.25–1.82	/	/
$\text{Na}_{11}\text{Sn}_2\text{P}_5\text{S}_{12}$ ^[47]	Yes	/	Yes	/	2.1	/	0.2 ^[43]	/	1.16–1.91	1.8	/
Na_3OCl ^[25]	/	/	/	/	1.376	0.063	0.23	0.428 ^[49]	/	/	/
Na_6SOI_2 ^[25]	Yes	Yes	Yes	Yes	10.36	1.79	0.16	/	0–1.5	3.28	/
Na_4Ol_2 ^[51]	Yes	Yes	Yes	Yes	0.058	4.17×10^{-4}	0.37	0.3–1.1 ^[62]	/	/	/
$\text{Na}_3\text{LiS}_{0.5}\text{O}_{0.5}\text{I}_2$ ^[51]	Yes	Yes	Yes	Yes	6.3	1.31	0.12	/	0–2.122	3.69	/
$\text{Na}_3\text{SeO}_4\text{F}_{0.5}\text{Cl}_{0.5}$ ^[52]	Yes	Yes	Yes	Yes	8.167	1.31	0.137	/	0.954–4.215	5.57	Inensitive

mentioning that only single crystal models have been considered in tractable AIMD simulation, without being able to account for grain/particle boundaries. This could lead to some extent of discrepancies between experimental data and theoretical predictions, depending on boundary qualities, possible segregation of chemical species etc. It was shown that such AIMD data are quite dependable once good bonding is achieved at boundaries, as grain boundaries are usually faster diffusional channels for condensed matter.^[56] Boundary issues cannot be addressed without using classic mesoscale methods involving coarser graining, when parameterization involving approximation have to be involved.

In terms of the ionic conductivity in solid batteries, competitive electrolytes also need to have acceptable ionic conductivity above 1 mS cm^{-1} at sub-zero Celsius temperatures. Such practical request cannot be met without the combined good room-temperature conductivity and low activation barrier, as is presented in Figure 8. It is worth noting that an activation energy not higher than 0.25 eV and a room-temperature conductivity over 5 mS cm^{-1} are needed to safeguard 1 mS cm^{-1} at -20°C .

3.5. Interfacial Challenges in All-Solid-State Battery

ASSBs face much greater challenges than conventional metal-ion batteries, since unlike in batteries with a liquid electrolyte, the ionic pathways in a solid cell can be easily interrupted. Major concerns include, poor physical contacts, undesirable reactions at interfaces, big stress induced by volumetric changes, electrochemical incompatibility with electrodes, and inadequate deformability etc.^[26,27] Among them, the matched electrochemical compatibilities between SSEs and electrodes are fundamental to avoid formation of undesirable electrolyte-electrode interphases. As is covered in the last section, the electrochemical windows can be readily assessed using DFT

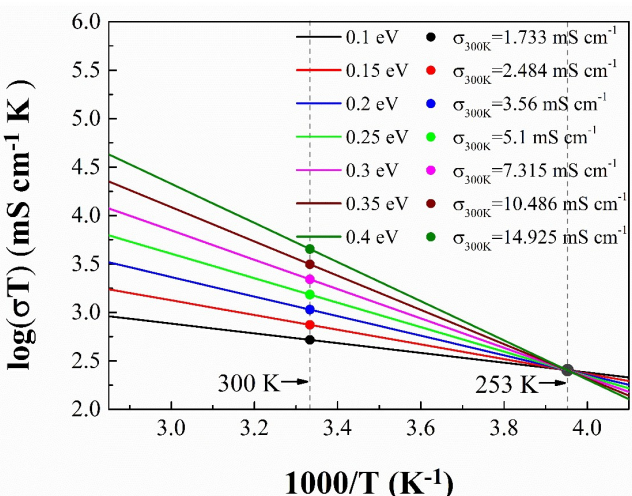


Figure 8. Requested ionic conductivity at room temperature and activation energy necessary to safeguard an acceptable conductivity of 1 mS cm^{-1} at -20°C .

simulation. Some efforts have been made in addressing the wider interfacial problems covering energetics behind interfacial reactions, electrochemical windows, mechanical properties, and so on.^[57,58,87,97,98]

As is recognized, a serious shortcoming for sulfide SSEs lies in their narrow electrochemical window vs. electrodes.^[99,100] As is summarized in Figure 9, sulfide SSEs, such as $\text{Na}_{10}\text{SnP}_2\text{S}_{12}$, Na_3PS_4 , and Na_3PSe_4 , are not electrochemically compatible against Na anode or reported cathodes. Reaction with the Na anode leads to the formation of Na_3P , Na_2S , etc., at the interface, which are poor conductors to alkali ions. The reduction potentials for such sulfides-based SSEs against Na are around 1.5 V, and their oxidation potentials are only around 2 V. Protective coatings need to be developed for their application to sustainable solid batteries. One notes from the theoretical modeling in the former section, inter-compatible SSE materials can be identified via extensive simulation tasks suitable for high-throughput materials genome engineering. It is worth pointing out that the electrochemical windows method only addresses the voltage effect due to change of ion concentration at the electrode-electrolyte interfaces. Interfacial reactions would also involve possible phase transformation due to inter-diffusion, which is largely metastable due to the limited temperature experienced in batteries.

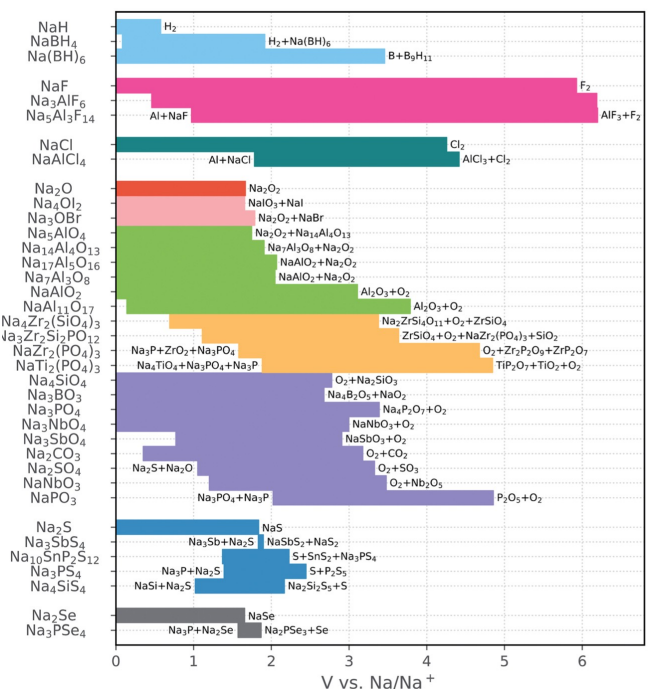


Figure 9. Calculated electrochemical stability windows of Na solid-state electrolyte candidates. The compounds are grouped by anion (the binaries are included for reference); the different oxide subgroups are distinguished by different colors. Reproduced from Ref. [99] with permission. Copyright (2019) The Authors.

4. Conclusions and Perspective

Here, we have reviewed recent advances in formulating solid electrolytes for sodium-ion batteries. DFT modeling has been shown to be a powerful tool to cover both materials stability and functionality essential for battery materials, and some highly attractive materials have been formulated in recent years. In addition to oxides and sulfides, recently formulated hali-chalcogenides based on anti-perovskite type of structures are enormously attractive in terms of high ionic conductivity, low activation energy, improved stabilities to ambient air and remarkably wide electrochemical windows.

The fundamental basis for dependable materials formulation lies in its largely reliable accuracy in predicting the cohesive energy of condensed matter, which in turn dictates a wide range of properties covering electrochemical characteristics, ionic transportation, phonon entropy for free energy, lattice parameters, elastic tensor and so on. The recognition that calculation of the cohesive energy can be largely fulfilled without using non-local functionals makes such DFT simulation highly attractive even for high throughput materials genome projects when limitation of computing costing is necessary. Calculation of band structures will usually need to consider non-local functionals, due to involvement of excited quantum states.

One notices that DFT methods can only handle relatively small systems, so that it is mainly confined to single crystals or slab interfaces. Scaling up of DFT to cover polycrystalline materials is extremely challenging due to limitation in current computing capability. To such aspects of real materials, coarse graining is needed. For example, DFT can be linked to classic molecular dynamics for meso-scale simulation at affordable computational cost. Machine learning can be involved for initial screening, with DFT tasks incorporated for fine-tuning of parameterization. Combination of DFT with CALPHAD could enable thermodynamic simulation in large multi-component systems, with wider consideration in the space covering temperature-composition-pressure and even external fields.

More efforts need to be directed towards predicting mechanical formability, which is key for developing materials suitable for simplified processing and lowered cost. Good plasticity is also critical to interfacial compatibility, high quality particle boundary formation in solid electrolytes, and the overall structural integrity of solid battery cells.

Acknowledgements

This work is supported in part by the Overseas Talents Program of China, the Zhengzhou Materials Genome Institute, the National Natural Science Foundation of China (No. 51001091, 51571182, 111174256, 91233101, 51602094, 11274100), the Fundamental Research Program from the Ministry of Science and Technology of China (no. 2014CB931704), and the Program for Science & Technology Innovation Talents in the Universities of Henan Province (18HASTIT009).

Conflict of Interest

The authors declare no conflict of interest.

Keywords: first-principle materials formulation • density functional theory • sodium-ion battery • solid electrolyte • electrochemistry

- [1] M. Armand, J. M. Tarascon, *Nature* **2008**, *451*, 652–657.
- [2] B. Dunn, H. Kamath, J. M. Tarascon, *Science* **2011**, *334*, 928–935.
- [3] B. Scrosati, J. Hassoun, Y. Sun, *Energy Environ. Sci.* **2011**, *4*, 3287–3295.
- [4] P.-J. Lian, B.-S. Zhao, L.-Q. Zhang, N. Xu, M.-T. Wu, X.-P. Gao, *J. Mater. Chem. A* **2019**, *7*, 20540–20557.
- [5] N. Nitta, F. Wu, J. T. Lee, G. Yushin, *Mater. Today* **2015**, *18*, 252–264.
- [6] V. Palomares, P. Serras, I. Villaluenga, K. B. Hueso, J. Carretero-González, T. Rojo, *Energy Environ. Sci.* **2012**, *5*, 5884–5901.
- [7] A. Eftekhari, *J. Power Sources* **2004**, *126*, 221–228.
- [8] X. Fan, R. R. Gaddam, N. A. Kumar, X. Zhao, *Adv. Energy Mater.* **2017**, *7*, 1700317.
- [9] Z. Wang, G. Shao, *J. Mater. Chem. A* **2018**, *6*, 6830–6839.
- [10] L. Zhang, L. Chen, X. Zhou, Z. Liu, *Adv. Energy Mater.* **2015**, *5*, 1400930.
- [11] J. H. Jo, Y. Aniskevich, J. Kim, J. U. Choi, H. J. Kim, Y. H. Jung, D. Ahn, T. Y. Jeon, K. S. Lee, S. H. Song, H. Kim, G. Ragoisha, A. Mazanik, E. Streltsov, S. T. Myung, *Adv. Energy Mater.* **2020**, *10*, 2001595.
- [12] J. Hwang, S. Myung, Y. Sun, *Chem. Soc. Rev.* **2017**, *46*, 3529–3614.
- [13] X. Chen, X. Shen, T.-Z. Hou, R. Zhang, H.-J. Peng, Q. Zhang, *Chem* **2020**, *6*, 2242–2256.
- [14] X. Chen, Y.-K. Bai, X. Shen, H.-J. Peng, Q. Zhang, *J. Energy Chem.* **2020**, *51*, 1–6.
- [15] K. Takada, *Acta Mater.* **2013**, *61*, 759–770.
- [16] M. Tatsumisago, M. Nagao, A. Hayashi, *J. Asian Ceram. Soc.* **2018**, *1*, 17–25.
- [17] Q. Wang, P. Ping, X. Zhao, G. Chu, J. Sun, C. Chen, *J. Power Sources* **2012**, *208*, 210–224.
- [18] G. Liu, D. Xie, X. Wang, X. Yao, S. Chen, R. Xiao, H. Li, X. Xu, *Energy Storage Mater.* **2019**, *17*, 266–274.
- [19] X. Han, Y. Gong, K. (K.) Fu, X. He, G. T. Hitz, J. Dai, A. Pearse, B. Liu, H. Wang, G. Rubloff, Y. Mo, V. Thangadurai, E. D. Wachsman, L. Hu, *Nat. Mater.* **2017**, *16*, 572–579.
- [20] N. Kamaya, K. Homma, Y. Yamakawa, M. Hirayama, R. Kanno, M. Yonemura, T. Kamiyama, Y. Kato, S. Hama, K. Kawamoto, A. Mitsui, *Nat. Mater.* **2011**, *10*, 682–686.
- [21] H. Deiseroth, S. Kong, H. Eckert, J. Vannahme, C. Reiner, T. Zaiß, M. Schlosser, *Angew. Chem. Int. Ed.* **2008**, *47*, 755–758; *Angew. Chem.* **2008**, *120*, 767–770.
- [22] A. Sakuda, A. Hayashi, M. Tatsumisago, *Sci. Rep.* **2013**, *3*, 2261.
- [23] T. Asano, A. Sakai, S. Ouchi, M. Sakaida, A. Miyazaki, S. Hasegawa, *Adv. Mater.* **2018**, *2*, 1803075.
- [24] L. Zhou, C. Y. Kwok, A. Shyamsunder, Q. Zhang, X. Wu, L. F. Nazar, *Energy Environ. Sci.* **2020**, *13*, 2056–2063.
- [25] Y. Yu, Z. Wang, G. Shao, *J. Mater. Chem. A* **2018**, *6*, 19843–19852.
- [26] Y. Lu, L. Li, Q. Zhang, Z. Niu, J. Chen, *Joule* **2018**, *2*, 1747–1770.
- [27] C. Zhao, L. Liu, X. Qi, Y. Lu, F. Wu, J. Zhao, Y. Yu, Y. Hu, L. Chen, *Adv. Energy Mater.* **2018**, *8*, 1703012.
- [28] Y. Y. Yao, J. T. Kummer, *J. Inorg. Nucl. Chem.* **1967**, *29*, 2453–2475.
- [29] N. Baffier, J. C. Badot, P. Colombar, *Mater. Res. Bull.* **1981**, *16*, 259–265.
- [30] S. Lee, D. Lee, S. Lee, S. Han, S. Lee, S. Lim, *Bull. Mater. Sci.* **2016**, *39*, 729–735.
- [31] X. Lu, G. Xia, J. P. Lemmon, Z. Yang, *J. Power Sources* **2010**, *195*, 2431–2442.
- [32] A. Hooper, *J. Phys. D* **1977**, *10*, 1487–1496.
- [33] K. B. Hueso, M. Armand, T. Rojo, *Energy Environ. Sci.* **2013**, *6*, 734–749.
- [34] Z. Yang, J. Zhang, M. C. W. Kintner-Meyer, X. Lu, D. Choi, J. P. Lemmon, J. Liu, *Chem. Rev.* **2011**, *111*, 3577–3613.
- [35] N. Anantharamulu, K. K. Rao, G. Rambabu, B. V. Kumar, V. Radha, M. Vithal, *J. Mater. Sci.* **2011**, *46*, 2821–2837.
- [36] Z. Zhang, Z. Zou, K. Kaup, R. Xiao, S. Shi, M. Avdeev, Y. Hu, D. Wang, B. He, H. Li, X. Huang, L. F. Nazar, L. Chen, *Adv. Energy Mater.* **2019**, *9*, 1902373.
- [37] S. Song, H. M. Duong, A. M. Korsunsky, N. Hu, L. Lu, *Sci. Rep.* **2016**, *6*, 32330.

- [38] Z. Zhang, Q. Zhang, J. Shi, Y. S. Chu, X. Yu, K. Xu, M. Ge, H. Yan, W. Li, L. Gu, Y. Hu, H. Li, X. Yang, L. Chen, X. Huang, *Adv. Energy Mater.* **2017**, 7, 1601196.
- [39] H. Park, K. Jung, M. Nezafati, C. S. Kim, B. Kang, *ACS Appl. Mater. Interfaces* **2016**, 8, 27814–27824.
- [40] A. Hayashi, K. Noi, N. Tanibata, M. Nagao, M. Tatsumisago, *J. Power Sources* **2014**, 258, 420–423.
- [41] N. J. J. de Klerk, M. Wagelmaker, *Chem. Mater.* **2016**, 28, 3122–3130.
- [42] W. D. Richards, T. Tsujimura, L. J. Miara, Y. Wang, J. C. Kim, S. P. Ong, I. Uechi, N. Suzuki, G. Ceder, *Nat. Commun.* **2016**, 7, 11009.
- [43] Z. Zhang, E. Ramos, F. Lalère, J. Assoud, K. Kaup, P. Hartman, L. F. Nazar, *Energy Environ. Sci.* **2018**, 11, 87–93.
- [44] H. Huang, H. Wu, X. Wang, B. Huang, T.-Y. Zhang, *Phys. Chem. Chem. Phys.* **2018**, 20, 20525–20533.
- [45] M. Duchardt, U. Ruschewitz, S. Adams, S. Dehnen, B. Roling, *Angew. Chem. Int. Ed.* **2018**, 57, 1351–1355; *Angew. Chem.* **2018**, 130, 1365–1369.
- [46] Y. Zhu, X. He, Y. Mo, *J. Mater. Chem. A* **2016**, 4, 3253–3266.
- [47] J. Liu, Z. Lu, M. B. Effat, F. Ciucci, *J. Power Sources* **2019**, 409, 94–101.
- [48] Y. Zhu, Y. Mo, *Angew. Chem. Int. Ed.* **2020**, 59, 17472–17476.
- [49] Y. Wang, Q. Wang, Z. Liu, Z. Zhou, S. Li, J. Zhu, R. Zou, Y. Wang, J. Lin, Y. Zhao, *J. Power Sources* **2015**, 293, 735–740.
- [50] E. Ahiavi, J. A. Dawson, U. Kudu, M. County, M. S. Islam, O. Clemens, C. Masquelier, T. Famprakis, *J. Power Sources* **2020**, 471, 228489.
- [51] Y. Yu, Z. Wang, G. Shao, *J. Mater. Chem. A* **2019**, 7, 10483–10493.
- [52] Y. Yu, Z. Wang, G. Shao, *J. Mater. Chem. A* **2019**, 7, 21985–21996.
- [53] H. Xu, M. Xuan, W. Xiao, Y. Shen, Z. Li, Z. Wang, J. Hu, G. Shao, *ACS Appl. Mater. Interfaces* **2019**, 2, 6288–6294.
- [54] M. H. Braga, J. A. Ferreira, V. Stockhausen, J. E. Oliveira, A. El-Azab, *J. Mater. Chem. A* **2014**, 2, 5470–5480.
- [55] C. Yan, R. R. Xu, J. Qin, H. Yuan, Y. Y. Xiao, L. L. Xu, J. Huang, *Angew. Chem. Int. Ed.* **2019**, 58, 15235–15238.
- [56] M. Xuan, W. Xiao, H. Xu, Y. Shen, Z. Li, S. Zhang, Z. Wang, G. Shao, *J. Mater. Chem. A* **2018**, 6, 19231–19240.
- [57] H. Xu, Y. Yu, Z. Wang, G. Shao, *Energy Environ. Mater.* **2019**, 2, 234–250.
- [58] H. Xu, W. Xiao, Z. Wang, J. Hu, G. Shao, *J. Energy Chem.* **2020**, DOI: 10.1016/j.jechem.2020.11.008, 10.1016/j.jechem.2020.1011.1008.
- [59] T. J. Whalen, G. J. Tennenhouse, C. Meyer, *J. Am. Ceram. Soc.* **1974**, 57, 497–498.
- [60] J. P. Boilot, G. Collin, P. Colombari, *J. Solid State Chem.* **1988**, 73, 160–171.
- [61] R. S. Gordon, G. R. Miller, B. J. McEntire, E. D. Beck, J. R. Rasmussen, *Solid State Ionics* **1981**, 3, 243–248.
- [62] J. Zhu, Y. Wang, S. Li, J. W. Howard, J. Neuefeind, Y. Ren, H. Wang, C. Liang, W. Yang, R. Zou, C. Jin, Y. Zhao, *Inorg. Chem.* **2016**, 55, 5993–5998.
- [63] C. W. Glass, A. R. Oganov, N. Hansen, *Comput. Phys. Commun.* **2006**, 175, 713–720.
- [64] A. R. Oganov, C. W. Glass, *J. Chem. Phys.* **2006**, 124, 244704.
- [65] A. Togo, F. Oba, I. Tanaka, *Phys. Rev. B* **2008**, 78, 134106.
- [66] K. Parlinski, Z. Q. Li, Y. Kawazoe, *Phys. Rev. Lett.* **1997**, 78, 4063–4066.
- [67] N. Saunders, A. P. Miodownik in *CALPHAD (Calculation of Phase Diagrams): A Comprehensive Guide*, Vol. 1 (Eds.: R. W. Cahn), Elsevier Science Ltd, **1998**.
- [68] A. Jain, K. A. Persson, G. Ceder, *APL Mater.* **2016**, 4, 053102.
- [69] A. Jain, S. P. Ong, G. Hautier, W. Chen, W. D. Richards, S. Dacek, S. Cholia, D. Gunter, D. Skinner, G. Ceder, K. A. Persson, *APL Mater.* **2013**, 1, 011002.
- [70] X. Zhao, Z. Zhang, X. Zhang, B. Tang, Z. Xie, Z. Zhou, *J. Mater. Chem. A* **2018**, 6, 2625–2631.
- [71] Z. Wang, H. Xu, M. Xuan, G. Shao, *J. Mater. Chem. A* **2018**, 6, 73–83.
- [72] Z. Deng, Z. Zhu, I.-H. Chu, S. P. Ong, *Chem. Mater.* **2016**, 29, 281–288.
- [73] M. V. Agnihotri, S. H. Chen, C. Beck, S. J. Singer, *J. Phys. Chem. B* **2014**, 118, 8170–8178.
- [74] G. Henkelman, B. P. Uberuaga, H. Jónsson, *J. Chem. Phys.* **2000**, 113, 9901–9904.
- [75] G. Henkelman, H. Jónsson, *J. Chem. Phys.* **2000**, 113, 9978–9985.
- [76] Z. Wang, X. Xia, M. Guo, G. Shao, *ACS Appl. Mater. Interfaces* **2016**, 8, 35298–35307.
- [77] Z. Wang, B. Lei, X. Xia, Z. Huang, K. P. Homewood, Y. Gao, *J. Phys. Chem. C* **2018**, 122, 2589–2595.
- [78] Z. Wang, M. Deng, X. Xia, Y. Gao, G. Shao, *Energy Environ. Mater.* **2018**, 1, 174–178.
- [79] Z. Wang, G. Shao, *J. Mater. Chem. A* **2017**, 5, 21846–21857.
- [80] X. He, Y. Zhu, A. Epstein, Y. Mo, *Npj Comput. Mater.* **2018**, 4, 18.
- [81] J. B. Bachman, S. Muy, A. Grimaud, H.-H. Chang, N. Pour, S. F. Lux, O. Paschos, F. Maglia, S. Lupart, P. Lamp, L. Giordano, Y. Shao-Horn, *Chem. Rev.* **2015**, 116, 140–162.
- [82] J. Heyd, G. E. Scuseria, M. Ernzerhof, *J. Chem. Phys.* **2003**, 118, 8207–8215.
- [83] J. Heyd, G. E. Scuseria, M. Ernzerhof, *J. Chem. Phys.* **2006**, 124, 219906.
- [84] Y. Mo, S. P. Ong, G. Ceder, *Chem. Mater.* **2011**, 24, 15–17.
- [85] G. L. W. Hart, R. W. Forcade, *Phys. Rev. B* **2008**, 77, 224115.
- [86] A. V. D. Walle, G. Ceder, *J. Phase Equilib.* **2002**, 23, 348–359.
- [87] Y. Ma, *Energy Environ. Mater.* **2018**, 1, 148–173.
- [88] S. Singh, I. Valencia-Jaime, O. Pavlic, A. H. Romero, *Phys. Rev. B* **2018**, 97, 054108.
- [89] R. Hill, *Proc. Phys. Soc. London Sect. A* **1952**, 65, 349–354.
- [90] F. Mouhat, F. Coudert, *Phys. Rev. B* **2014**, 90, 224104.
- [91] J. B. Goodenough, H. Y. P. Hong, J. A. Kafalas, *Mater. Res. Bull.* **1976**, 11, 203–220.
- [92] H. Y.-P. Hong, *Mater. Res. Bull.* **1976**, 11, 173–182.
- [93] M. Guin, F. Tietz, *J. Power Sources* **2015**, 273, 1056–1064.
- [94] H. Fang, P. Jena, *Proc. Natl. Acad. Sci. USA* **2017**, 114, 11046–11051.
- [95] W. Li, Z. Wang, F. Deschler, S. Gao, R. H. Friend, A. K. Cheetham, *Nat. Rev. Mater.* **2017**, 2, 16099.
- [96] Y. Liang, G. Shao, *RSC Adv.* **2019**, 9, 7551–7559.
- [97] W. Xiao, H. Xu, M. Xuan, Z. Wu, Y. Zhang, X. Zhang, S. Zhang, Y. Shen, G. Shao, *J. Energy Chem.* **2021**, 53, 147–154.
- [98] H. Huang, Y. Yang, C. Chi, H.-H. Wu, B. Huang, *J. Mater. Chem. A* **2020**, 8, 22816–22827.
- [99] V. Lacivita, Y. Wang, S. Bo, G. Ceder, *J. Mater. Chem. A* **2019**, 7, 8144–8155.
- [100] Y. Tian, T. Shi, W. D. Richards, J. Li, J. C. Kim, S. Bo, G. Ceder, *Energy Environ. Sci.* **2017**, 10, 1150–1166.

Manuscript received: December 12, 2020

Revised manuscript received: January 17, 2021

Accepted manuscript online: January 18, 2021

Version of record online: February 8, 2021